

University of Dayton

eCommons

---

Chemical and Materials Engineering Faculty  
Publications

Department of Chemical and Materials  
Engineering

---

9-17-2019

## Optimization and Structural Stability of Gold Nanoparticle–Antibody Bioconjugates

Robert T. Busch  
*University of Dayton*


Farzia Karim  
*University of Dayton*

John Weis  
*University of Dayton*

Yvonne Sun  
*University of Dayton, ysun02@udayton.edu*

Chenglong Zhao  
*University of Dayton, czhao1@udayton.edu*

Follow this and additional works at: [https://ecommons.udayton.edu/cme\\_fac\\_pub](https://ecommons.udayton.edu/cme_fac_pub)

 Part of the [Other Chemical Engineering Commons](#), and the [Other Materials Science and Engineering Commons](#)

---

### eCommons Citation

Busch, Robert T.; Karim, Farzia; Weis, John; Sun, Yvonne; and Zhao, Chenglong, "Optimization and Structural Stability of Gold Nanoparticle–Antibody Bioconjugates" (2019). *Chemical and Materials Engineering Faculty Publications*. 222.

[https://ecommons.udayton.edu/cme\\_fac\\_pub/222](https://ecommons.udayton.edu/cme_fac_pub/222)

This Article is brought to you for free and open access by the Department of Chemical and Materials Engineering at eCommons. It has been accepted for inclusion in Chemical and Materials Engineering Faculty Publications by an authorized administrator of eCommons. For more information, please contact [mschlengen1@udayton.edu](mailto:mschlengen1@udayton.edu), [ecommons@udayton.edu](mailto:ecommons@udayton.edu).

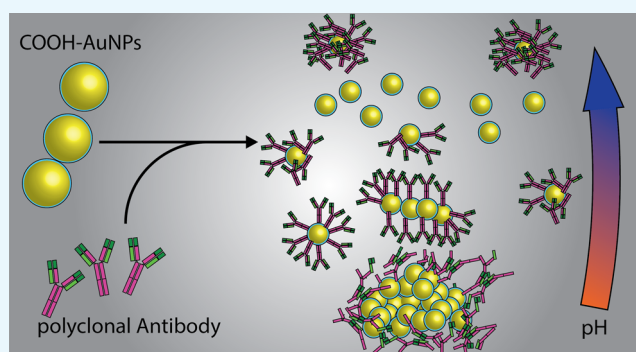
# Optimization and Structural Stability of Gold Nanoparticle–Antibody Bioconjugates

Robert T. Busch,<sup>†</sup> Farzia Karim,<sup>‡</sup> John Weis,<sup>§</sup> Yvonne Sun,<sup>§,⊥</sup> Chenglong Zhao,<sup>‡,||</sup> and Erick S. Vasquez<sup>\*,†,⊥,Ⓜ</sup>

<sup>†</sup>Department of Chemical and Materials Engineering, <sup>‡</sup>Department of Electro-Optics and Photonics, <sup>§</sup>Department of Biology, <sup>⊥</sup>Integrative Science and Engineering Center, and <sup>||</sup>Department of Physics, University of Dayton, 300 College Park, Dayton, Ohio 45469, United States

## Supporting Information

**ABSTRACT:** Gold nanoparticles (AuNPs) bound with biomolecules have emerged as suitable biosensors exploiting unique surface chemistries and optical properties. Many efforts have focused on antibody bioconjugation to AuNPs resulting in a sensitive bioconjugate to detect specific types of bacteria. Unfortunately, bacteria thrive under various harsh environments, and an understanding of bioconjugate stability is needed. Here, we show a method for optimizing *Listeria monocytogenes* polyclonal antibodies bioconjugation mechanisms to AuNPs via covalent binding at different pH values, from 2 to 11, and 2-(*N*-morpholino)ethanesulfonic acid (MES), 3-(*N*-morpholino)propanesulfonic acid, NaOH, HCl conditions. By fitting Lorentz curves to the amide I and II regions, we analyze the stability of the antibody secondary structure. This shows an increase in the apparent breakdown of the antibody secondary structure during bioconjugation as pH decreases from 7.9 to 2. We find variable adsorption efficiency, measured as the percentage of antibody adsorbed to the AuNP surface, from 17 to 27% as pH increases from 2 to 6 before decreasing to 8 and 13% at pH 7.9 and 11, respectively. Transmission electron microscopy (TEM) analysis reveals discrepancies between size and morphological changes due to the corona layer assembly from antibody binding to single nanoparticles versus aggregation or cluster self-assembly into large aggregates. The corona layer formation size increases from 3.9 to 5.1 nm from pH 2 to 6, at pH 7.9, there is incomplete corona formation, whereas at pH 11, there is a corona layer formed of 6.4 nm. These results indicate that the covalent binding process was more efficient at lower pH values; however, aggregation and deactivation of the antibodies were observed. We demonstrate that optimum bioconjugation condition was determined at pH 6 and MES buffer-type by indicators of covalent bonding and stability of the antibody secondary structure using Fourier transform-infrared, the morphological characteristics and corona layer formation using TEM, and low wavelength shifts of ultraviolet–visible after bioconjugation.



## INTRODUCTION

In recent years, gold nanoparticle (AuNP) bioconjugation has emerged as a pivotal technique for the advanced detection of pathogens. AuNPs have proven to be an ideal vessel for bioconjugation and biosensor purposes due to their unique surface characteristics, optical properties, stability, and consistency.<sup>1–5</sup> Using surface modification techniques, many types of molecules such as peptides, oligonucleotides, enzymes, DNA, and antibodies can be attached to AuNPs through physisorption or chemisorption.<sup>6–8</sup> From these molecules, antibodies have emerged as an ideal targeting mechanism for antigen-specific pathogen detection due to their increasing availability, quality, and specificity.<sup>9</sup>

To utilize antibodies in biosensors and sensing devices, favorable substrate interactions must be developed.<sup>10</sup> Antibody molecules can be attached to the surface-functionalized AuNP via chemisorption, targeting various functionalities, such as

cysteine or amine groups, or electrostatic interactions, utilizing ionic or hydrophobic interactions.<sup>2,11</sup> The antibody-bound AuNPs must be stable under a broad range of wet chemistry conditions (e.g., pH, salt concentration, and type, or temperature); therefore, a covalent bond is preferred.<sup>10,12</sup> Currently, two major covalent bioconjugation strategies are being investigated. Targeted immobilization through terminal thiols creates consistent stable Au–S bonds and has been shown to facilitate stable structural chemisorption of bovine serum albumin (BSA) and tunable orientation via pH manipulation.<sup>11,13</sup> In direct competition, robust amide bonds through pegylated carboxyl groups around AuNPs have

Received: July 22, 2019

Accepted: August 21, 2019

Published: September 9, 2019

provided oriented functionalization with heightened functional site accessibility.<sup>14</sup>

This type of covalent bonding is regularly established via carbodiimide crosslinker chemistry using 1-(3-dimethylamino-propyl)-3-ethylcarbodiimide hydrochloride-*N*-hydroxysuccinimide (EDC/NHS).<sup>6,15</sup> Previously, this method has been used to effectively bind primary amines on antibodies onto carboxyl end-functionalized AuNPs.<sup>2</sup> However, all antibodies have multiple primary amine binding sites largely originating from lysine residues.<sup>14,16</sup> Primary amines on an antibody molecule serve as the recognition sites that can detect and bind to antigens. The range of orientations and packing densities resulted from EDC/NHS crosslinking of nanoparticles to antibodies at the primary amine termini could potentially result in antibodies with compromised binding to their target antigens.<sup>17</sup> Despite tangible drawbacks, such as undesired antibodies orientation, EDC/NHS binding has the distinct advantage of providing a stable and consistent covalent bond. Several studies have optimized the wet chemistry conditions to favor antibody orientation when bound to a surface.<sup>13,14,18</sup> For instance, previous research on two-dimensional substrates suggests that the wet conditions, such as pH, ionic concentration, and buffer-type, influence the antibody orientation and binding capacity.<sup>19</sup> For sensitive detection using AuNPs coupled with antibodies, it is necessary to optimize the antibody AuNP bioconjugation process to maintain stability and provide a functional orientation of the antibodies on the nanoparticle surface.

Bioconjugation conditions between the biomolecule and nanoparticles via covalent bonding must be consistent, predictable, and stable for quality AuNP-antibody interactions. To achieve binding with optimum antibody orientation, the solvent conditions such as buffer-type, pH, and ionic concentration play a critical role. As an example, when using buffer solutions, the structural integrity of the polyclonal antibodies (pAb) must be maintained as it can greatly affect EDC/NHS carbodiimide crosslinker reactions. Noncoordinating zwitterionic buffers are ideal selections for maintaining a stable environment about the particle and avoid coordination with the AuNPs.<sup>20</sup> The buffer pH will then play a significant role in changing the surface charge effects of the AuNPs and, subsequently, the rate and quality of the binding reaction.<sup>21,22</sup> This change in the surface charge can be monitored via  $\zeta$ -potential probing over the pH range.<sup>23</sup> After covalent bioconjugation, an inherent increase in  $\zeta$ -potential is expected from the utilized pAb containing a less negative charge, which is an indicator of successful corona layer assembly.<sup>24</sup>

To understand the complex interactions during the antibody corona formation, analyzing the specific type of adsorption mechanisms of the biomolecules to the nanoparticles is fundamental.<sup>25,26</sup> It is expected that following binding, average particle size will increase due to aggregation for several reasons. First, the natural interaction of cysteine with metal nanoparticles causes dissolution.<sup>27</sup> Second, portions of the protein unfold upon bioconjugation and due to pH changes. This unfolding allows the proteins to interact, which induces the aggregation of particles via protein interaction.<sup>11,28–30</sup> Using spectroscopic techniques, such as the highly active ultraviolet-visible (UV-vis) and Fourier transform-infrared (FT-IR) spectra produced by AuNPs at different binding stages, the interactions between the biomolecules and the AuNP surface can be precisely described. Particularly, FT-IR allows for

descriptions of pAb-AuNP complex interactions in the corona layer assemblies.<sup>31,32</sup> This technique allows the analysis of the stability changes in the secondary structure of the biomolecule.<sup>33–36</sup> Hence, specific information on the structural effects of pAb-AuNPs interactions at specific solvent conditions can be obtained. Simultaneously, UV-vis is useful to provide insights to the kinetics and the stability of the pAb-coated AuNPs.<sup>37,38</sup>

In this study, we determine the balance between efficiency and stability of the bound antibody, as a function of solvent pH (pH 2–11) and buffer-type, to carboxyl-functionalized AuNPs using EDC/NHS chemistry. Carboxyl end-functionalized AuNPs were bioconjugated to *Listeria monocytogenes* targeting polyclonal immunoglobulin G class antibodies (pAb) under different wet chemistry conditions. To determine optimal pH and buffer conditions for the *L. monocytogenes* pAb-AuNP bioconjugation, the balance between stability and binding capacity of the AuNPs was assessed by analyzing kinetic measurements during the covalent binding of the pAb to the AuNP. This analysis is done by conducting time-dependent hydrodynamic diameter, UV absorbance, and  $\zeta$ -potential measurements during the adsorption process. Then, by utilizing infrared spectroscopic analysis, a description of the potential conformational and secondary structure changes to the pAb upon the formation of the pAb-AuNP complex over the tested pH and buffer conditions is presented. Finally, the self-assembly and the effects of the adsorption process on the morphological characteristics of pAb-AuNP conjugates are analyzed and discussed by observing the corona layer formation through TEM imaging.

## ■ MATERIALS AND METHODS

**Materials.** *N*-(3-dimethylaminopropyl)-*N'*-carbodiimide (EDC, 97%), *N*-hydroxysuccinimide (NHS, 98%), 3-(*N*-morpholino)propanesulfonic acid (MOPS, 99.5%), 3-(*N*-morpholino)propanesulfonic acid sodium salt (99.5%), 2-(*N*-morpholino)ethanesulfonic acid (MES, 99.5%), 2-(*N*-morpholino)ethanesulfonic acid sodium salt (99%), hydroxylamine 50 weight % in H<sub>2</sub>O, isopropyl alcohol (IPA, 98%) were purchased from Sigma-Aldrich (St. Louis, MO). Hydrochloric Acid, 10% v/v aqueous solution (HCl), was purchased from Alfa Aesar (Ward Hill, MA). Gold nanospheres (40 nm, BioReady, carboxyl, 20 OD, 5 mL, water) were obtained from NanoComposix (San Diego, CA). A rabbit polyclonal antibody against *L. monocytogenes* (PIPA130487) was purchased from Fisher Scientific and used without further purification. All reagents were used as received. Ultrapure type-1 water (18 M $\Omega$  cm) was acquired from an Elga PURELAB purification system and was used for all buffer preparations. Thermo Scientific Pierce 96-Well Plates, Product No. 15041 was used for bicinchoninic acid (BCA) assay. Bovine serum albumin (BSA) standard kit was purchased from Thermo Fisher catalog #23225.

**AuNPs Carbodiimide Crosslinking Procedure.** Carboxylated gold nanoparticles (40 nm, COOH-AuNPs) were used for their consistent optical extinction peak at 525 nm prior to bioconjugation.<sup>39</sup> Solutions of EDC and NHS were prepared at 2 and 10 mg/mL, respectively, using water. Carboxylated gold nanoparticles (200  $\mu$ L of 40 nm, COOH-AuNPs) were added to CCPO microcentrifuge tubes, which were previously washed with isopropyl alcohol and deionized (DI) water. Desired buffer solution (1 mL) was added to the 200  $\mu$ L of carboxylated gold nanoparticles to begin pH control.

**Table 1.** ATR FT-IR Lorentz Peak Wavenumber Assignments ( $\text{cm}^{-1}$ ) of the Protein Secondary Structure for Correlation to Figures 4 and S9

secondary structure	peak FT-IR wavenumber $\text{cm}^{-1}$			
$\beta$ -sheets	$1623 \pm 2$	$1636 \pm 4$	$1676 \pm 4$	$1688 \pm 2$ (weak)
$\alpha$ -helix	$1654 \pm 2$			
random coil/turns	$1646 \pm 3$	$1664 \pm 2$	$1688 \pm 2$	

EDC ( $40 \mu\text{g}$ ),  $20 \mu\text{L}$  of  $2 \text{ mg/mL}$  of the solution, was added to  $1.2 \text{ mL}$  of AuNP solution. This solution was vortexed at  $1000 \text{ RPM}$  at room temperature for  $10 \text{ min}$ . NHS ( $80 \mu\text{g}$ ),  $8 \mu\text{L}$  of  $10 \text{ mg/mL}$  of the solution, was added to the EDC/AuNPs solution. The solution was vortexed at  $1000 \text{ RPM}$  at room temperature for  $10 \text{ min}$  followed by centrifugation at  $15000 \text{ RCF}$  for  $10 \text{ min}$  at  $10^\circ\text{C}$ . The supernatant was carefully removed, and the remaining pellet was resuspended with  $200 \mu\text{L}$  of the respective buffer prepared at the desired pH value. Resuspension was performed by sonicating the solution for  $5 \text{ min}$  and vortex mixing for  $5 \text{ min}$  at  $1000 \text{ RPM}$ . This washing procedure was repeated twice followed by off-line dynamic light scattering (DLS) runs using  $20 \mu\text{L}$  of the suspension in  $1.5 \text{ mL}$  of DI water. The remaining nanoparticle suspension was diluted with  $1 \text{ mL}$  of the buffer solution and placed in a  $2 \text{ mL}$  microcuvette in the UV-vis analyzer. Antibody solution ( $8 \mu\text{L}$  of  $1 \text{ mg/mL}$ ) was then added to the AuNP colloidal suspension for a minimum of  $90 \text{ min}$  or until the time-resolved UV-vis spectra no longer experienced peak changes, reaching adsorption equilibrium. The solution was centrifuged, and the supernatant was removed and retained to test the antibody adsorption efficiency using UV-vis measurements, as described in the next section. The AuNP pellet was resuspended in  $200 \mu\text{L}$  of DI water, and  $1 \mu\text{L}$  of the quencher ( $50\%$  hydroxylamine) was added to the solution. The solution was then split into two  $100 \mu\text{L}$  samples, centrifuged at  $15000 \text{ RCF}$  for  $10 \text{ min}$  at  $10^\circ\text{C}$ , and resuspended in different solvents. One sample was resuspended with DI water, whereas the other was resuspended with the reaction pH buffer. This washing step was performed three times. pAb binding via noncarbodiimide crosslinking was performed identically to the reaction above excluding the EDC/NHS chemistry steps as a control experiment to assess electrostatic interactions.

**BCA Protein Assay.** Triplicates of BSA standards were prepared at  $0, 1, 5, 10, 25,$  and  $50 \mu\text{g/mL}$ . Weight ratios of  $50$  parts of BCA reagent A with  $1$  part of BCA reagent B were mixed for immediate use. To a  $96$ -well plate,  $25 \mu\text{L}$  of each standard and each tested condition was added followed by  $200 \mu\text{L}$  of the mixed BCA reagent. The plate was covered and incubated for  $55 \text{ min}$  at  $37^\circ\text{C}$ . Absorbance was measured at  $562 \text{ nm}$  both prior to and after incubation to ensure that results were not skewed due to leftover particles in the supernatant.

**Ultraviolet-visible Spectroscopy (UV-vis).** Ultraviolet-visible spectra of the prepared AuNPs were measured with a Lambda 900 UV/VIS/NIP spectrometer in the range of  $300$ – $1000 \text{ nm}$ . A polystyrene  $2 \text{ mL}$  semimicrocuvette was used to hold  $1.2 \text{ mL}$  and to record the spectra. An initial spectrum was taken of the AuNPs in each of the reaction solvents. Data acquisition was run continuously, whereas the pAb reaction was occurring after the EDC/NHS crosslinking steps. Data was taken every  $5 \text{ min}$  for  $90 \text{ min}$  or until a UV absorbance of  $0$  was recorded at the  $525$  or  $585 \text{ nm}$  wavelength. To analyze the degree of aggregation, the aggregation index (AI) eq 1 was used

$$(\text{AI}) = A_{585}/A_{525} \quad (1)$$

with  $A_{525}$  being the peak absorption value at  $525 \text{ nm}$  and  $A_{585}$  being the peak absorption value at  $585 \text{ nm}$ . Values greater than  $1$  were considered aggregated.<sup>24</sup>

Additional UV-vis measurements were used to determine the concentration of unbound antibody remaining in the supernatant via the BCA protein assay method. This equation is shown in the Supporting Information, eq S1.

The pAb binding efficiency was then calculated using eq 2

$$\text{efficiency \%} = ([\text{pAb}]_0 - [\text{pAb}])/[\text{pAb}]_0 \quad (2)$$

where  $\text{pAb}_0$  is the initial concentration of the antibody added to the solution and  $\text{pAb}$  is the concentration found via the calibration curves from the supernatant after three washes. The calibration curves were developed by taking the absorbance reading at  $562 \text{ nm}$  and fitting linear regression of absorbance in AU vs the concentration for diluted BSA standards was used in this study.

After determining the binding efficiency, final UV-vis curves were taken to determine the wavelength at the maximum absorbance in arbitrary units. This wavelength is reported as the localized surface plasmon resonance (LSPR).

**Fourier Transform-Infrared Spectrometry (FT-IR).** FT-IR was measured by a Nicolet iS50 FT-IR spectrometer using an attenuated total reflection (ATR) attachment (Smart Golden Gate, ZnSe lens, Thermo Electron North America LLC). A minimum of  $128$  scans was collected, with the background spectrum collected after each sample. A liquid nitrogen-cooled (MCT-A) detector with a CdTe window ZnSe crystal was utilized, and data was gathered using the OMNIC Software Suite v7.3. COOH-AuNPs, pAb-AuNPs, and pAb samples of  $10 \mu\text{L}$ s were placed directly onto the ATR crystal and allowed to dry for approximately  $40 \text{ min}$  until a thin film remained. The reference spectrum for each sample was taken under identical conditions after the crystal was cleaned with isopropyl alcohol. Second derivative spectra and Lorentz curves were generated using OriginPro v.9.1 by subtraction of the water spectra such that a straight baseline was obtained between  $2000$  and  $1750 \text{ cm}^{-1}$ .<sup>40,41</sup> Following this procedure, a Lorentz fitting of the amide I and amide II regions for each sample was obtained with the Lorentzian band  $A(\nu)$  expressed as eq 3

$$A(\nu) = (A_0 * \gamma^2)/[\gamma^2 + (\nu - \nu_0)^2] \quad (3)$$

where  $A_0$  is the maximum absorbance of the individual Lorentz peak,  $\nu_0$  is the frequency of the maximum, and  $\nu$  is the half-width at half height of the individual Lorentz peak. Multiple Lorentz peaks were summed to fit each curve peak as closely as possible. Following fitting, the second derivative is assigned. Taking the second derivative of each curve allows for more sensitive detection of influential peaks. All peak assignments were performed in the OriginPro 9.1 software.

To analyze binding effects at each pH condition using FT-IR spectra, it is critical to adjust for water in this region ( $1640$

$\text{cm}^{-1}$ ). The water spectra are collected under identical methodology as the pAb–AuNP samples and are used to subtract from the pAb–AuNP spectra to minimize 1750–2000  $\text{cm}^{-1}$  wavenumber region.<sup>40,41</sup> Following this procedure, a Lorentz curve fitting is performed on the resulting spectra. Lorentz peak locations are assigned by adding peaks listed in Table 1 iteratively to find optimal fitting parameters, where optimization is determined by obtaining an R-squared value close to 1 (Figure 4). The second derivative of each of the fitted curves is then taken to compare the peak location and determine the most influential peaks by relative size.

**$\zeta$ -Potential Measurements.** Average  $\zeta$ -potential was measured using an Anton Paar Litesizer 500 instrument with a minimum of 200 and a maximum of 600 runs until a standard deviation of less than 0.1 mV was achieved at 25 °C. Samples of 200  $\mu\text{L}$ :1 mL dilution, placed in a folded capillary  $\zeta$ -cell were acquired from Anton Paar. A control sample, using the COOH–AuNPs in each of the reaction solutions, was taken along with control points using 0.5 pH value increments of the reaction buffers within their usable range to fill the  $\zeta$ -potential curve. Additionally, the  $\zeta$ -potential was taken of the particles after pAb bioconjugation diluted with ultrapure type-1 water, MOPs buffer adjusted to a pH of 7, NaOH adjusted to a pH of 11, and HCl adjusted to a pH of 3.

**Dynamic Light Scattering (DLS).** The intensity, effective, and number diameters of the AuNPs were measured using a NanoBrook 90Plus with a red (640 nm) laser and a 90° scattering angle. A quartz cuvette was used for all measurements. For each sample, five DLS measurements were conducted with 10 repetitions for each measurement, and average results are reported. The off-line DLS samples were prepared as a 1:20 dilution by volume from the prepared solution with DI water. DLS was collected before each bioconjugation, before the addition of the antibody to the solution, and after the completion of bioconjugation for each buffer pH condition studied.

**Transmission Electron Microscopy (TEM) Images.** Transmission electron microscopy (TEM) images were collected with a Hitachi H-7600 TEM instrument at 100 kV. CF300-copper grids and Fontax #16 tweezers obtained from Electron Microscope Sciences were washed in IPA immediately prior to use. A nanoparticle colloid (5  $\mu\text{L}$ ) was added to a copper carbon mesh grid followed by 3  $\mu\text{L}$  of IPA to break the surface tension. The tweezers, holding the grid, were then placed in a vacuum chamber for 15 min. The sample was then removed from the chamber and allowed to dry for an additional 30 min at room temperature before use in the TEM. The analysis of the particle and corona layer size was performed using the ImageJ analyze particle function.

## RESULTS AND DISCUSSION

**Time-Dependent Studies of Polyclonal Antibody (pAb), Gold Nanoparticle (AuNP) Structures.** UV–vis, DLS, and  $\zeta$ -potential are used to assess the in situ condition of the pAb in the solution and the effects of the pAb–AuNP formation at each pH condition (HCl-2, MES-4.5, MES-6, MOPs-7.9, NaOH-11) performed in this study. The COOH–AuNPs are used as a control study at each pH condition. An increase in the aggregation index (AI) as compared to the COOH–AuNPs measured during the final UV–vis spectrum for each pAb binding onto AuNPs at the respective pH condition reveals a decrease in stability (Figure S1). AI is

indicative of the aggregate formation or primary particles forming crystalline structures and fusing together.<sup>42</sup>

At a pH 2 condition, a peak wavelength increase of over 100 nm, paired with an AI above 1, suggests complete aggregation. The MES-4.5 and MES-6 conditions saw the lowest peak wavelength shifts of  $12.5 \pm 2.5$  and  $10 \pm 2.5$  nm, respectively, which is within the previously reported shift increase for bioconjugation with AuNPs.<sup>39,43,44</sup> The pAb–AuNP MOPs-7.9 exhibited minimal changes in UV–vis spectra with respect to the COOH–AuNPs, as observed in Figure 1. A higher

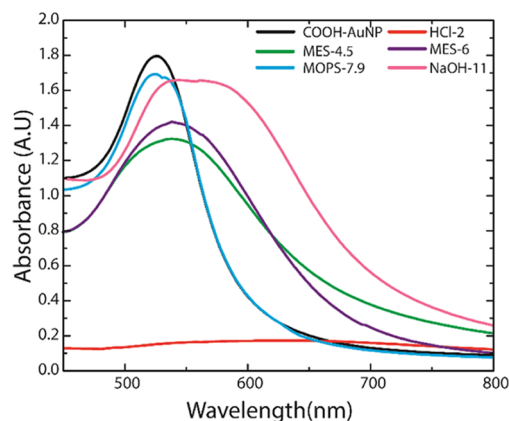


**Figure 1.** UV–vis spectra for resulting pAb–AuNP structures at each bioconjugation procedure.

wavelength increase is observed at NaOH-11 condition with a  $17.5 \pm 2$  nm redshift. This result is slightly above the expected wavelength increase for the formation of pAb–AuNP<sup>43</sup> and is an indication of aggregation.<sup>24,39</sup> Also, the aggregation is confirmed with the AI nearing 1 for the NaOH-11 condition and the broad nature of the UV–vis spectra, which is attributed to the linear aggregation due to dipole interactions.<sup>45</sup>

After antibody bioconjugation, DLS for each pAb–AuNP showed an increase in diameter due to the antibody bioconjugation and surface passivation. The maximum expected increase from a fully developed corona of the antibody on its longest axis is  $\sim 30$  nm from DLS assuming that no other effects are present, as reported elsewhere.<sup>46</sup> At all pH values, larger variations in the particle size are observed for the pAb–AuNP bioconjugates. This discrepancy is likely indicative of the formation of large combined particles through weak physical interactions such as aggregation and agglomeration.<sup>42,47,48</sup> Additionally, the use of pAbs has a primary disadvantage of cross-reactivity between the monoclonal antibodies within the total immunoglobulin system.

When the corona layer does not achieve full coverage of the COOH–AuNPs, dimers and trimers are likely to form to create stable intermediates due to dipole interactions as asymmetric distributions of charges form. Additionally, adsorption of antibodies into the corona layer without targeted covalent binding but via electrostatic interactions or binding through cysteine groups can cause sensitivity of the particle to solution conditions resulting in instability of reactive moieties and decreased antigen-binding capacity.<sup>49</sup> This undesirable binding can occur largely due to the net charge dominating early interactions between proteins and AuNPs in situ.<sup>50</sup> Each of the tested conditions increases in the diameter size more than 30 nm, a result regularly seen during the formation of

pAb–AuNP nanoprobe.<sup>44,51</sup> This is a primary disadvantage to this type of the bioconjugation method as crosslinking of the carbodiimide bridge can attribute to the increase in the particle size.<sup>17</sup> The DLS diameters by number match the  $\zeta$ -potential changes (Figures 2 and S2, S3), with the highest  $\Delta\zeta$ -potential

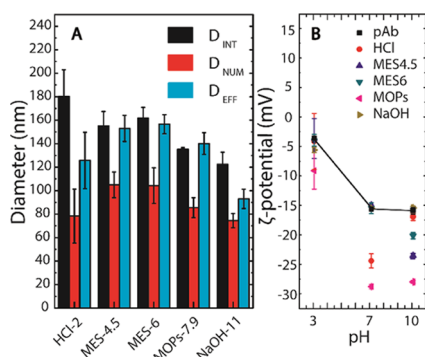


**Figure 2.** (A) DLS by intensity, number, and the effective diameter of pAb–AuNPs demonstrates an increase in the particle size after each bioconjugation procedure while suspended in water. (B)  $\zeta$ -Potential of pAb–AuNPs after bioconjugation is performed suspended in pH 3, pH 7, and pH 10 solutions.

values corresponding to the largest size increase. The exception occurs at the NaOH-11 condition, which maintains the lowest diameter after the bioconjugation procedure. The discrepancies between the number, effective, and intensity diameters are indicative of each condition experiencing a few large aggregates.<sup>46</sup>

The pAb–AuNPs show a stronger resiliency or ability to hold various  $\zeta$ -potential charges to stabilize electrostatic interactions at broader pH ranges after binding. This is suggested by positive  $\zeta$ -potentials at the low pH conditions for each of the prepared pAb–AuNP excluding MOPs-7.9. Furthermore, a drastic pH dependence is shown by the MES-4.5, MES-6, and NaOH conditions, while matching the  $\zeta$ -potential of the pAb at the neutral pH 7 condition.<sup>52</sup> Antibody corona formation resulted in a net increase in  $\zeta$ -potential from all pH bioconjugation values when compared to the COOH–AuNPs (Figures S4 and S5), confirming at minimum, partial adsorption of antibody at each condition.<sup>53</sup> When the pAb–AuNPs are tested at pH 3, a positive  $\zeta$ -potential is observed, whereas all other bioconjugation pH values maintain negative values with varied pH increase. As the particles are coated with proteins, the  $\zeta$ -potential becomes more stable at lower pH values by acting as buffer coatings with positive  $\zeta$ -potential at pH below the protein isoelectric point (pI).<sup>52</sup> Denaturing of the secondary structure is likely to occur at low pH values allowing for epitope interactions between the proteins.<sup>30</sup> Hence, the positive  $\zeta$ -potential value is not a perfect indicator for pAb–AuNP stability.<sup>54</sup>

Following bioconjugation,  $\zeta$ -potential changes with respect to COOH–AuNPs at the neutral pH 7 condition see a net increase in charge:  $\Delta\zeta_{\text{HCl-2}} = 9.71 \pm 1.6$ ,  $\Delta\zeta_{\text{MES-4.5}} = 17.4 \pm 0.4$ ,  $\Delta\zeta_{\text{MES-6}} = 17.01 \pm 1.3$ ,  $\Delta\zeta_{\text{MOPs-7.9}} = 4.08 \pm 0.5$ , and  $\Delta\zeta_{\text{NaOH-11}} = 18.06 \pm 0.43$  (Figures 2B and S3). Differences in the changes are likely due to a mixture of packing density bonding and orientation of the antibody. As the packing density increases, the diffuse layer increases in size resulting in diffusion limitation of the positively charged ions. After adsorption of the pAb, the large negative charge of the

carboxyl groups is no longer able to assist in decreasing the  $\zeta$ -potential of the particles. Finally, after covalent bonding, the positive charges of the lysine residues on the pAbs will attract negative ions. Depending on the orientation of the binding and, subsequently, the amount of residues oriented away from the particle, the  $\zeta$ -potential increases.<sup>43</sup> The slipping plane will experience a larger positive shift when the F(ab')<sub>2</sub> regions are oriented away from the particle or when the particle is in the face-on configuration. Based on these results, the MES-4.5, MES-6, and NaOH-11 conditions maintain the most ideal  $\zeta$ -potential increase.

#### Chemical Characterization of pAb–AuNP Structures.

Neat COOH–AuNP, pAb at each pH condition and in water, the pAb–AuNP synthesized at each pH condition, and pAb–AuNP synthesized without the addition of EDC/NHS chemistry steps are characterized using attenuated total reflection (ATR) FT-IR to analyze the chemical changes after bioconjugation (Figure 3). Primary indicators for

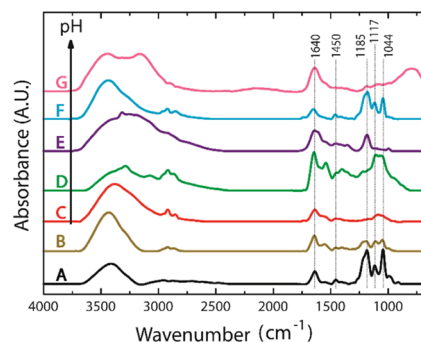


**Figure 3.** Normalized FT-IR curve for each pAb–AuNPs: (A) Neat *L. monocytogenes* pAb, (B) Neat COOH–AuNPs, (C) pAb–AuNPs HCl-2, (D) pAb–AuNPs MES-4.5, (E) pAb–AuNPs MES-6, (F) pAb–AuNPs MOPs-7.9, (G) pAb–AuNPs NaOH-11.

carbodiimide-initiated covalent bonding will be peak formations in the amide regions across the FT-IR spectrum. Specifically, the formation of a sharp peak in the amide A region, near 3300 cm<sup>-1</sup>, and an increase in the peak height in the amide II regions are strong indicators of covalent bonding.<sup>55,56</sup> The formation of this peak is expected for an amide bond during the crosslinking resulting in an N–H stretch.<sup>57</sup> Additionally, the complex nature of the side chains of proteins containing many types of amide and amine bonds requires many newly formed amide bonds must be present to create a sharp peak atop the wide protein curves between 3000 and 3750 cm<sup>-1</sup>.<sup>57,58</sup> This type of wide peak is seen in the amide A region of the neat pAb (Figure 3A) and at all pH conditions excluding the NaOH-11 condition (Figures S6 and S7). The neat pAb spectrum shows notable absorption peaks at 1044, 1117, 1185, and 1455 cm<sup>-1</sup> in the fingerprint and amide III regions as well as a peak at 1638 cm<sup>-1</sup> and a shoulder at 1554 cm<sup>-1</sup> in the amide I and II regions, respectively.

The AuNP has similar absorption peaks in this wavenumber region. Specific peaks for the AuNPs are observed at 1051, 1110, 1191, 1403, 1464, and 1643 cm<sup>-1</sup>. A complete peak assignment to both the neat pAb and AuNPs is listed in Table S1.<sup>32,59–61</sup> The pH and buffer conditions used during bioconjugation influence the fingerprint region causing broadening and peak shifts by affecting the adsorption of the pAb to the COOH–AuNP. Due to the large amount of absorption peak overlap between the pAb and COOH–AuNP, a more

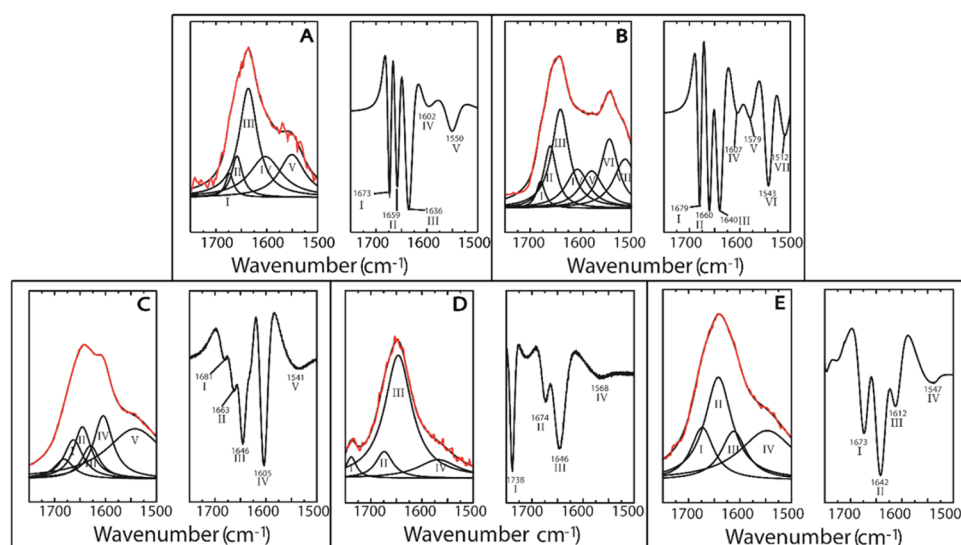


**Figure 4.** Lorentz fit and the second derivative for the amide I and II region of: (A) HCl-2, (B) MES-4.5, (C) MES-6, (D) MOPs-7.9, (E) NaOH-11.

detailed analysis of the peak assignment is needed to understand conformational changes of the antibodies after binding onto the AuNPs surface. The amide A region of the full FT-IR spectrum suggests that both the MES-4.5 and MES-6 conditions caused the formation of the carbodiimide bridge and, thus, covalent bonding between the pAb and COOH-AuNP (Figure 3D–E). This shows a notch at  $\sim 3300\text{ cm}^{-1}$  associated with N–H stretching from the formation of a secondary amine during binding via Schiff base reduction, a reaction which is highly dependent on pH as well as the peak increase in the amide II band expected of binding.<sup>57</sup>

Comparing these peaks to the pAb tested at each respective pH condition, major peak changes occur throughout the FT-IR spectra at each pAb–AuNP condition excluding the MOPs-7.9 condition (Figure S6). For further comparison to ensure that peak changes are a resultant of the carbodiimide crosslinking, each pAb–AuNP condition was tested with the absence of EDC/NHS (Figure S7). These spectra contain peak wavenumber differences for each spectrum in the amide II and fingerprint regions, excluding the MOPs-7.9 condition. Furthermore, the MES-4.5 and MES-6 conditions lack a sharp peak in the amide A region, which is present in the carbodiimide crosslinker pAb–AuNPs. Strengthening the claim that covalent bonding or at a minimum successful formation of the carbodiimide crosslinker has occurred.

The secondary structures of proteins, such as  $\alpha$ -helix,  $\beta$ -sheets, turns, and unordered structures, can be described by deconstruction of the additive curves in the amide I and II regions.<sup>62</sup> Specific stretching and bending of the peptide backbone in amide I, II, and III bands have proven an effective technique for describing changes in these structures.<sup>63</sup> The amide I band has become the most consistent, widely used region for conformational changes, whereas the amide II band can describe hydrogen exchanges and relative amounts of adsorbed protein.<sup>34,64</sup> Specific wavenumber assignments in the amide I region ( $1600\text{--}1720\text{ cm}^{-1}$ ) have been shown to be descriptors for protein conformations (Table 1).<sup>41</sup>

Once each sample is adjusted for the influence of water, the resulting spectra for each of the pAb–AuNP assembly conditions are compared to the neat pAb, the pAb at their respective pH condition, the COOH–AuNP and the pAb–

AuNPs conjugated without the EDC/NHS chemistry steps. The carboxyl-functionalized groups surrounding the AuNPs influence the curves as the amide I band corresponds with all C=O bonds and, as such, the definition of the changes in the pAb structure will be muddled. There are three peaks assigned in the amide I region ( $1600\text{--}1700\text{ cm}^{-1}$ ) shown with Lorentz fitting of the neat antibody (Figure S8A). The 1641 and 1623  $\text{cm}^{-1}$  peaks are assigned to  $\beta$ -sheet secondary structures, whereas the 1666  $\text{cm}^{-1}$  peak is assigned to the  $\beta$ -turns of the secondary structure. In the nonsmoothed curve, there is a slight shoulder near the 1651  $\text{cm}^{-1}$  mark, which is likely the low amount of  $\alpha$ -helix contained in the pAb structure.<sup>31</sup> This is in agreement with literature values as the majority (>60%) of the pAb is  $\beta$ -sheets.<sup>55</sup> In the amide II region, there is a single peak at 1543  $\text{cm}^{-1}$  (N–H), representative of a primary amine deformation.<sup>57</sup>

Each of these peaks is in direct competition with one of the pAb peaks. This can cause interference in analyzing the Lorentz curves. The second derivative of the final curve allows for a method of increased sensitivity for peak locations and acts as a convolution indicator for overlapping peaks.<sup>65</sup> As such, the two curves are used in tandem for each bioconjugation condition to describe pAb binding and structural changes. The pAb–AuNP conjugated at a HCl-2 pH condition fit five peaks at 1673, 1659, 1636, 1602, and 1550  $\text{cm}^{-1}$  (Figure 4A). These peaks correspond to the presence of  $\beta$ -sheet, random coil, turns, and, to a lesser extent,  $\alpha$ -helix. Overall these peaks suggest the presence of pAb; however, the peak shifts also suggest that the pAb may have denatured.<sup>66</sup> As a result, an over-representation of random coil/ $\beta$ -turn type curves is observed that is unique to the carbodiimide crosslinking adsorption of the HCl-2 condition, as these peak assignments are not seen in the pAb or the pAb–AuNPs test without EDC/NHS at the HCl-2 condition (Figures S9 and S10).

At a slightly higher pH, MES-4.5 condition, improved pAb binding conditions are determined (Figure 4B). The amide I band peaks are observed at 1679, 1660, and 1640  $\text{cm}^{-1}$ . These peaks are assigned to  $\beta$ -sheets,  $\beta$ -turns or random coils, and  $\beta$ -sheets or the carboxyl group on the COOH–AuNP, respectively. Interestingly, results suggest the presence of both uncoated COOH–AuNP and pAb. Like the HCl-2 pAb–

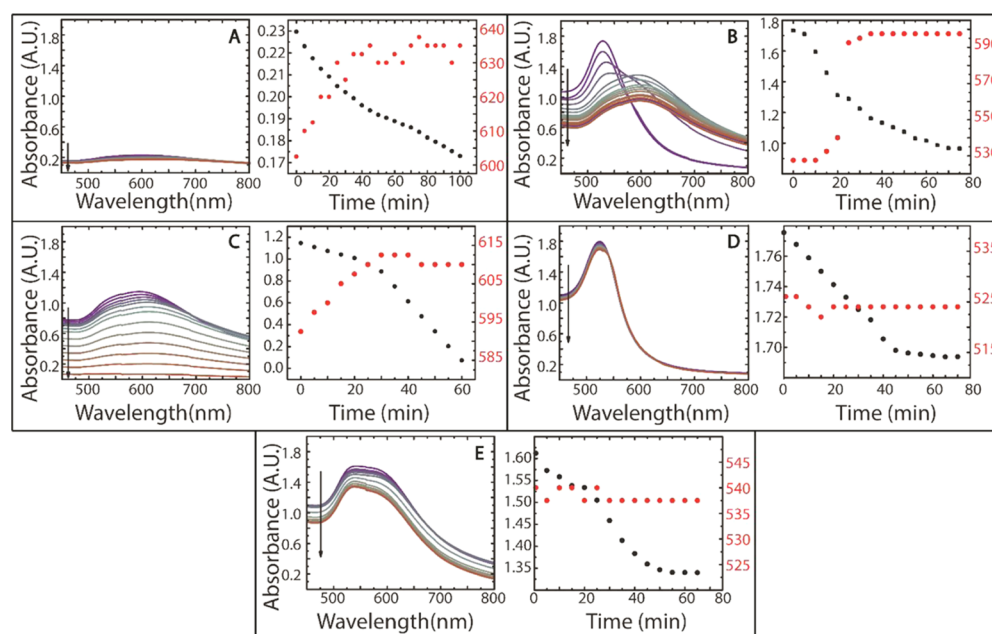


**Figure 5.** Time-resolved UV-vis spectra with absorbance during the reaction; tracking absorbance peak (black, arbitrary units) and wavelength shift (red, nm) of: (A) HCl-2, (B) MES-4.5, (C) MES-6, (D) MOPs-7.9, (E) NaOH-11.

AuNP, there is an over-representation of  $\beta$ -turns or random coils suggesting that the pAb may have denatured. These structural changes are unique to the MES-4.5 pAb-AuNPs carbodiimide binding, as shown by the pAb and pAb-AuNPs tested without EDC/NHS (Figures S11 and S12). Conversely, the amide II region contains a sharp relative peak increase of the primary amine at  $1543\text{ cm}^{-1}$ , which directly matches the peak value found for the neat pAb. The direct peak value match may be indicative of consistent and more uniform stretching of this portion of the pAb structure.<sup>56</sup> Furthermore, consistent stretching would suggest that binding of similar lysine groups on the pAb has occurred, possibly giving the pAb consistent orientation if the pAb electrostatically adsorbed prior to the covalent bonding. This is shown to have a higher likelihood of occurring, though is not guaranteed, at lower pH values.<sup>19,64,67</sup>

pAb-AuNP bioconjugates at the MES-6 pH condition have amide I peaks at  $1681, 1663, 1646\text{ cm}^{-1}$  with an additional peak at  $1630\text{ cm}^{-1}$  (Figure 4C). The MES-6 pAb-AuNP also contains the amide II curve at  $1541\text{ cm}^{-1}$  suggesting the presence of pAb with minimal traces of COOH-AuNPs an indicator of carboxyl group coverage. The lack of increase in the  $\beta$ -turns or random coils in the second derivative indicated stability in the pAb, which is not seen in MES-4.5 or HCl-2 pAb-AuNPs. Furthermore, these structural changes are not seen in the pAb alone or the pAb-AuNPs conjugated without EDC/NHS, a strong indicator that these results are unique to the carbodiimide crosslinking at the MES-6 condition (Figures S13 and S14). Bonding multiple lysine groups in different locations will cause a wide peak as the stretching of each group will carry different wavenumber frequencies.<sup>64</sup> As a result, the broad amide I peak for the MES-6 bioconjugation suggests multiple structural formations and binding orientations. The lack of consistent binding orientation is further supported by the broad shoulder of the  $1541\text{ cm}^{-1}$  peak, an indicator of lower selectivity.<sup>68</sup>

Both the amide I and amide II bands for the pAb-AuNP bioconjugate at the MOPs-7.9 condition show Lorentz fits and

second derivatives like those seen for the untreated AuNP with peaks at  $1738, 1674, 1646, \text{ and } 1568\text{ cm}^{-1}$  (Figure 4D). This result suggests that there is little to no pAb present, which is supported by the lack of change seen in the final UV-vis spectra (Figure 1) as well as the similarities in the amide A bands and fingerprint regions of the full spectra. Additionally, pAb alone and pAb-AuNPs tested without EDC/NHS show drastically different Lorentz peak locations (Figures S15 and S16).

At the most basic solution condition, the NaOH-11, the pAb-AuNPs held four peaks at  $1673, 1642, 1612, \text{ and } 1547\text{ cm}^{-1}$  (Figure 4E). The assignment of these peaks is comparable to pAb, with the second derivative having three major peaks in the amide I region. The peaks are noticeably broader and have been shifted slightly; however, there is not enough evidence that covalent binding has occurred. Rather the basic pH value caused the pAb to physically adsorb to the surface in a noncovalent manner to cover the negative charge of the carboxyl groups around the surface of the AuNP.<sup>17</sup> This relies on the pH value being high enough to overcome the negative repulsion of the particles shown by  $\zeta$ -potential (Figure 2B). The shifted values are also in line with the curve fitting data from the literature of immunoglobulin G (IgG)-type antibodies adsorbed onto silica surfaces.<sup>41</sup> Furthermore, similar peak locations are seen in the pAb-AuNP NaOH-11 condition tested without the EDC/NHS chemistry steps (Figures S17 and S18).

For FT-IR analysis, the MES-4.5 and MES-6 conditions display the strongest characteristics for pAb-AuNP bioconjugation. The MES-4.5 condition suggests that pH and buffer selection can affect the ability to consistently bind lysine residues on the pAb. In this instance, selectivity causes slight destabilization of the secondary structure, indicated by an over-representation of  $\beta$ -turns or random coil peaks. The MES-6 condition provides indicators of secondary structure stability while maintaining peak locations consistent with the covalent bond formation for the pAb-AuNP.



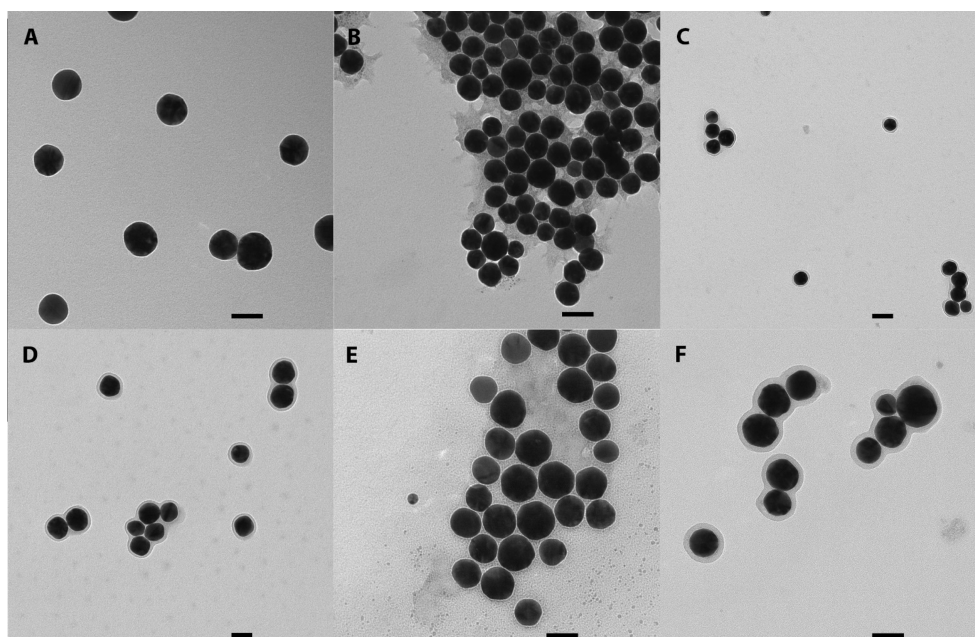


**Figure 6.** TEM scale length corresponds to 40 nm in length images of: (A) Neat COOH–AuNPs, (B) pAb–AuNPs HCl-2, (C) pAb–AuNPs MES-4.5, (D) pAb–AuNPs MES-6, (E) pAb–AuNPs MOPs-7.9, (F) pAb–AuNPs NaOH-11.

**Time-Dependent Antibody Binding Analysis of pAb–AuNPs.** Each of the time-dependent UV–vis spectra is taken after completing EDC/NHS crosslinker chemistry. After placing the treated nanoparticles at the respective solution condition, both the HCl-2 and NaOH-11 are partially aggregated prior the antibody binding step, as seen in the DLS measurement of the EDC/NHS step before pAb addition (Figure S19). Furthermore, aggregation is present prior to the crosslinker chemistry steps in the HCl-2 condition, apparent by the localized surface plasmon resonance (LSPR) wavelength initiating at greater than 600 nm as well as the initial DLS (Figures 5A and S2).<sup>24</sup> This cannot be attributed to the chemistry step but rather to aggregation caused by electrostatic interactions induced by the low pH value.<sup>69</sup>

The initial addition of pAb to the EDC/NHS-modified COOH–AuNP induced complete aggregation in the MES-6 condition shown by the LSPR absorbance reaching 0 after 95 min and the LSPR maximum wavelength maintaining at greater than 600 nm (Figure 5B). Partial aggregation in the MES-4.5 condition shown by the LSPR maximum wavelength maintaining at greater than 600 nm (Figure 5C). The time-dependent UV–vis spectra can be used to check for dispersion or maintaining particles in the solution without mixing, by having a final time-resolved absorbance greater than zero.<sup>70</sup> Aggregation and agglomeration characteristics among these samples are in direct competition with the covalent binding characteristics of the desired reaction and adsorption of antibodies to the surface of the particles.

The pAb–AuNP LSPR peak absorbance has red-shifted compared to the COOH–AuNP at all pH conditions except MOPs-7.9, where minimal changes in UV–vis spectra are observed. The NaOH-11 condition does not see a change in the peak wavelength over time after the shift from the EDC/NHS chemistry step (Figure 5D). The HCl-2, MES-4.5, MES-6 conditions have indicators of time-dependent adsorption, described by the peak wavelength shift of over 20 nm. The plateau of peak wavelength shifts is indicative of maximum packing for each condition, which is less effective at binding

antigens due to steric hindrance of the pAb.<sup>5,18</sup> As such, time-dependent studies can be used to estimate the packing density of the pAb–AuNP moving forward.

**Morphological Characterization of pAb–AuNP Bioconjugates.** Transmission electron microscopy (TEM) images show an increase in the corona layer assembly size for each pAb bioconjugation condition (Figures 6 and S20). The COOH–AuNPs (Figure 6A) are  $42 \pm 2$  nm in diameter. The HCl-2 condition (Figure 6B) is determined to be  $50 \pm 5$  nm, with signs of aggregation, agglomeration, and protein denaturation.<sup>1,71–73</sup> The average corona layer size is  $3.9 \pm 2$  nm, which suggests either denaturation of pAb, side-on or face-on orientation. The MES-4.5 (Figure 6C) and MES-6 (Figure 6D) buffer bioconjugation conditions are  $56 \pm 5$  nm, and  $51 \pm 4$  nm, respectively. Each shows indications of the stable pAb corona layer assembly with slight aggregation. The corona layer thicknesses for MES-4.5 and MES-6 buffer bioconjugation are  $4.6 \pm 1$  and  $5.1 \pm 1$  nm, respectively. Size increases are within the desired corona size (3–6 nm), which suggests that either side-on or face-on orientation is achieved. The 3–6 nm region is the ideal size change as flat-on and end-on orientations are the desired directional conformation, as the average value for the conjugate, part of which is not covered by pAb.<sup>5,17</sup> The MOPs-7.9 (Figure 6E) bioconjugation condition has a diameter of  $45 \pm 4$  nm with few signs of corona layer assembly and aggregation occurring. The MOPs-7.9 bioconjugation has negligible corona layer measured as  $0.4 \pm 0.3$  nm. This result suggests low levels of binding, corroborated by the low pAb efficiency described in Figure S2. The NaOH-11 condition is determined to be  $52 \pm 4$  nm with signs of aggregation and agglomeration. This condition maintains a corona layer of  $6.4 \pm 2$  nm slightly outside of the desired corona size. The discrepancies between the corona layer size found and the DLS size (Figure 2A) are likely due to the pAb–AuNPs displaying a tendency to agglomerate in the aqueous solution due to protein interaction.<sup>30,74</sup>

pAb adsorption efficiency (Figures S21 and S22) is determined via BCA protein assay's calibrated by optical

density curves for the concentration of pAb remaining in the supernatant. The HCl-2 condition results in an adsorption efficiency of 17%. This directly correlates to the expected increase in the corona layer size (Figure S8) compared to the MES-4.5 and MES-6 conditions. It is expected that the corona layer size would be directly and positively correlated to the antibody efficiency. For the HCl-2 condition, this contradiction may be due to the breakdown and aggregation of the pAb structure or unfavorable orientation of the pAb (Figure 6B). The MES-4.5 and MES-6 conditions are found to have the highest efficiencies at 28 and 27%, respectively, these values are relatively close and appear to corroborate the corona layer size previously discussed and shown in Figure S4. The MOPs-7.9 condition maintained a 7% efficiency, which corresponds to the low corona layer formation size shown in Figure S4. The NaOH-11 condition has the second-lowest efficiency at 13% while maintaining the highest corona layer size regardless of pAb aggregation or denaturation. Efficiency is found to be drastically different when tested with and without EDC/NHS to assess the effects of electrostatic interactions (Figure S22). The uptake of the pAb to the AuNP via carbodiimide crosslinking is most efficient at the MES-4.5 and MES-6 conditions. On the contrary, when bioconjugation is performed without EDC/NHS, the MOPs-7.9 condition has the highest pAb physisorption efficiency at 38%. Furthermore, pAb chemisorption efficiency decreases drastically for the HCl-2, NaOH-11, and MOPs-7.9 conditions (Figure S22). Thus, the two MES pH conditions are expected to have the highest packing density, which is in line with the TEM analysis, with the exception of the NaOH-11 condition.

The TEM images corroborate the results of the Lorentz FT-IR fittings, (Figures 3 and 4) showing corona layer assembly around each of the particles barring MOPs-7.9. Comparing the MOPs-7.9 condition with the DLS data (Figure 2A) shows an inherent increase in size due to interactions other than protein binding, which is minimal. The HCl-2 TEM images show apparent denaturation and aggregation of the pAb around the AuNP, indicated by the loose tendril-like chains, which are not tightly packed against the particles. Hence, the discrepancy between the corona layer size and high pAb adsorption efficiency is attributed to the large aggregates observed and the denatured pAbs at the HCl-2 condition. The particularly large corona layer assembly around the NaOH-11 AuNP is in line with the high pAb adsorption efficiency. This suggests that the NaOH-11 condition causes physical adsorption to occur, where pAb efficiency is higher than other conditions, and TEM corona formation is larger than 6 nm, which is expected for pH conditions much higher than the pAb pI.<sup>24</sup>

## CONCLUSIONS

This study details the effect of pH on the stability and binding nature of *L. monocytogenes* targeting polyclonal antibodies (pAb) to carboxyl-functionalized gold nanoparticles (COOH-AuNPs). The results shown here demonstrate the tunability of a well-established carbodiimide reaction for the pAb-AuNP formation based on binding efficiency, corona layer assembly type and size, and aggregate formation. The pAb-AuNP formation is found to maintain increased binding efficiency at the moderately low MES-4.5 and MES-6 test conditions as compared to alternative pH conditions. By comparison, efficiency due to electrostatic adsorptions shows the MOPs-7.9 maintaining the highest binding efficiency, shown by the calibration of pAb remaining in the supernatant. Corona layer

assembly is found to be ideally sized at the pH 4.5 and 6 conditions, while showing a large layer at pH 11, nonexistent at pH 7.9, and with protein denaturation at pH 2. The ATR-FT-IR for the pH 4.5 and 6 conditions suggests the formation of new covalent bonds, while maintaining stability throughout the amide I and II regions, key indicators of the pAb maintaining their structure. Conversely, the pH 11 condition shows signs only of physical adsorption. The aggregate formation causes complications when optimizing the pAb-AuNP complex formation. Overall, we demonstrate the exquisite balance to bind polyclonal antibodies to carboxyl-functionalized AuNP at different pH and buffer conditions. For pAb-AuNP bioconjugation, the MES-6 condition should be utilized despite the low binding efficiency obtained by UV-vis, due to indicators of covalent bonding and stability in the pAb secondary structure from FT-IR, corona layer formation and morphology of TEM, and the charge stabilization of  $\zeta$ -potential.

## ASSOCIATED CONTENT

### Supporting Information

The Supporting Information is available free of charge on the ACS Publications website at DOI: 10.1021/acsomega.9b02276.

Contains FT-IR peak assignments; analysis of neat COOH-AuNPs; analysis of neat pAb; analysis of pAb at each pH condition; analysis of electrostatically conjugated pAb-AuNPs at each pH condition; and  $\zeta$ -potential of the neat COOH-AuNPs (PDF)

## AUTHOR INFORMATION

### Corresponding Author

\*E-mail: [evasquez1@udayton.edu](mailto:evasquez1@udayton.edu).

### ORCID

Erick S. Vasquez: 0000-0002-4811-6155

### Funding

Funding available through the University of Dayton STEM Catalyst Initiative and the Graduate Student Summer Fellowship.

### Notes

The authors declare no competing financial interest.

## ACKNOWLEDGMENTS

The authors would like to thank the University of Dayton Chemistry Department and Dr Yoon Lee for access to the Anton Paar Litesizer 500.

## ABBREVIATIONS

pAb, polyclonal antibody; AuNP, gold nanoparticle; COOH-AuNPs, carboxylated gold nanoparticles; MES, 2-(*N*-morpholino) ethanesulfonic acid; MOPS, 3-(*N*-morpholino) propane-sulfonic acid; EDC, *N*-(3-(dimethylaminopropyl)-*N'*-carbodiimide); NHS, *N*-hydroxysuccinimide; LSPR, localized surface plasmon resonance; DLS, dynamic light scattering; UV-vis, ultraviolet-visible spectroscopy; FT-IR, Fourier transform-Infrared spectroscopy; TEM, Transmission electron microscopy; pI, isoelectric point; ATR, attenuated total reflection; IgG, immunoglobulin G

## REFERENCES

- (1) Alzoubi, F.; Al-Zoubi, J.; Alqadi, M.; Alshboul, H. A.; Aljarrah, K. Synthesis and Characterization of Colloidal Gold Nanoparticles Controlled by the PH and Ionic Strength. *Chin. J. Phys.* **2015**, *53*, 1–9.
- (2) Jazayeri, M. H.; Amani, H.; Pourfatollah, A. A.; Pazoki-Toroudi, H.; Sedighimoghaddam, B. Various Methods of Gold Nanoparticles (GNPs) Conjugation to Antibodies. *Sens. Bio-Sensing Res.* **2016**, *9*, 17–22.
- (3) Iosin, M.; Toderas, F.; Baldeck, P. L.; Astilean, S. Study of Protein-Gold Nanoparticle Conjugates by Fluorescence and Surface-Enhanced Raman Scattering. *J. Mol. Struct.* **2009**, *924–926*, 196–200.
- (4) Deol, S.; Weerasuriya, N.; Shon, Y. S. Stability, Cytotoxicity and Cell Uptake of Water-Soluble Dendron-Conjugated Gold Nanoparticles with 3, 12 and 17 Nm Cores. *J. Mater. Chem. B* **2015**, *3*, 6071–6080.
- (5) Fratila, R. M.; Mitchell, S. G.; Del Pino, P.; Grazu, V.; De La Fuente, J. M. Strategies for the Biofunctionalization of Gold and Iron Oxide Nanoparticles. *Langmuir* **2014**, *30*, 15057–15071.
- (6) Bartzczak, D.; Kanaras, A. G. Preparation of Peptide-Functionalized Gold Nanoparticles Using One Pot EDC/Sulfo-NHS Coupling. *Langmuir* **2011**, *27*, 10119–10123.
- (7) Tiwari, P.; Vig, K.; Dennis, V.; Singh, S. Functionalized Gold Nanoparticles and Their Biomedical Applications. *Nanomaterials* **2011**, *1*, 31–63.
- (8) Ciaurriz, P.; Fernández, F.; Tellechea, E.; Moran, J. F.; Asensio, A. C. Comparison of Four Functionalization Methods of Gold Nanoparticles for Enhancing the Enzyme-Linked Immunosorbent Assay (ELISA). *Beilstein J. Nanotechnol.* **2017**, *8*, 244–253.
- (9) Lipman, N. S.; Jackson, L. R.; Trudel, L. J.; Weis-Garcia, F. Monoclonal Versus Polyclonal Antibodies: Distinguishing Characteristics, Applications, and Information Resources. *ILAR J.* **2013**, *46*, 258–268.
- (10) Stephanopoulos, N.; Francis, M. B. Choosing an Effective Protein Bioconjugation Strategy. *Nat. Chem. Biol.* **2011**, *7*, 876–884.
- (11) Tsai, D. H.; Delrio, F. W.; Keene, A. M.; Tyner, K. M.; MacCuspie, R. I.; Cho, T. J.; Zachariah, M. R.; Hackley, V. A. Adsorption and Conformation of Serum Albumin Protein on Gold Nanoparticles Investigated Using Dimensional Measurements and in Situ Spectroscopic Methods. *Langmuir* **2011**, *27*, 2464–2477.
- (12) Bickerstaff, G. *Immobilization of Enzymes and Cells*; Springer Science & Business Media, 1996; Vol. 1.
- (13) Ruiz, G.; Tripathi, K.; Okyem, S.; Driskell, J. D. PH Impacts the Orientation of Antibody Adsorbed onto Gold Nanoparticles. *Bioconjugate Chem.* **2019**, *30*, 1182–1191.
- (14) Parolo, C.; De La Escosura-Muñiz, A.; Polo, E.; Grazú, V.; De La Fuente, J. M.; Merkoçi, A. Design, Preparation, and Evaluation of a Fixed-Orientation Antibody/Gold-Nanoparticle Conjugate as an Immunosensing Label. *ACS Appl. Mater. Interfaces* **2013**, *5*, 10753–10759.
- (15) Zhang, Q.; Li, R. X.; Chen, X.; He, X. X.; Han, A. L.; Fang, G. Z.; Liu, J. F.; Wang, S. Study of Efficiency of Coupling Peptides with Gold Nanoparticles. *Chin. J. Anal. Chem.* **2017**, *45*, 662–667.
- (16) Panowski, S.; Bhakta, S.; Raab, H.; Polakis, P.; Junutula, J. R. Site-Specific Antibody Drug Conjugates for Cancer Therapy. *mAbs* **2014**, *6*, 34–45.
- (17) Montenegro, J. M.; Grazu, V.; Sukhanova, A.; Agarwal, S.; de la Fuente, J. M.; Nabiev, I.; Greiner, A.; Parak, W. J. Controlled Antibody/(Bio-) Conjugation of Inorganic Nanoparticles for Targeted Delivery. *Adv. Drug Delivery Rev.* **2013**, *65*, 677–688.
- (18) Saha, B.; Evers, T. H.; Prins, M. W. J. How Antibody Surface Coverage on Nanoparticles Determines the Activity and Kinetics of Antigen Capturing for Biosensing. *Anal. Chem.* **2014**, *86*, 8158–8166.
- (19) Pei, Z.; Anderson, H.; Myrskog, A.; Dunér, G.; Ingemarsson, B.; Aastrup, T. Optimizing Immobilization on Two-Dimensional Carboxyl Surface: PH Dependence of Antibody Orientation and Antigen Binding Capacity. *Anal. Biochem.* **2010**, *398*, 161–168.
- (20) Ferreira, C. M. H.; Pinto, I. S. S.; Soares, E. V.; Soares, H. M. V. M. (Un)Suitability of the Use of PH Buffers in Biological, Biochemical and Environmental Studies and Their Interaction with Metal Ions—a Review. *RSC Adv.* **2015**, *5*, 30989–31003.
- (21) Ngo, V. K. T.; Nguyen, H. P. U.; Huynh, T. P.; Tran, N. N. P.; Lam, Q. V.; Huynh, T. D. Preparation of Gold Nanoparticles by Microwave Heating and Application of Spectroscopy to Study Conjugate of Gold Nanoparticles with Antibody E. coli O157:H7. *Adv. Nat. Sci.: Nanosci. Nanotechnol.* **2015**, *6*, 3–10.
- (22) Boulos, S. P.; Davis, T. A.; Yang, J. A.; Lohse, S. E.; Alkilany, A. M.; Holland, L. A.; Murphy, C. J. Nanoparticle-Protein Interactions: A Thermodynamic and Kinetic Study of the Adsorption of Bovine Serum Albumin to Gold Nanoparticle Surfaces. *Langmuir* **2013**, *29*, 14984–14996.
- (23) Wang, Z.; Chen, Z.; Yang, L.; Tan, F.; Wang, Y.; Li, Q.; Chang, Y. I.; Zhong, C. J.; He, N. Effect of Surface Physicochemical Properties on the Flocculation Behavior of Bacillus Licheniformis. *RSC Adv.* **2017**, *7*, 16049–16056.
- (24) Yeo, E. L. L.; Chua, A. J. S.; Parthasarathy, K.; Yeo, H. Y.; Ng, M. L.; Kah, J. C. Y. Understanding Aggregation-Based Assays: Nature of Protein Corona and Number of Epitopes on Antigen Matters. *RSC Adv.* **2015**, *5*, 14982–14993.
- (25) Ansar, S. M.; Perera, G. S.; Gomez, P.; Salomon, G.; Vasquez, E. S.; Chu, I. W.; Zou, S.; Pittman, C. U.; Walters, K. B.; Zhang, D. Mechanistic Study of Continuous Reactive Aromatic Organothiol Adsorption onto Silver Nanoparticles. *J. Phys. Chem. C* **2013**, *117*, 27146–27154.
- (26) Vangala, K.; Siriwardana, K.; Vasquez, E. S.; Xin, Y.; Pittman, C. U.; Walters, K. B.; Zhang, D. Simultaneous and Sequential Protein and Organothiol Interactions with Gold Nanoparticles. *J. Phys. Chem. C* **2013**, *117*, 1366–1374.
- (27) Siriwardana, K.; Wang, A.; Gadogbe, M.; Collier, W. E.; Fitzkee, N. C.; Zhang, D. Studying the Effects of Cysteine Residues on Protein Interactions with Silver Nanoparticles. *J. Phys. Chem. C* **2015**, *119*, 2910–2916.
- (28) Dominguez-Medina, S.; Kisley, L.; Tauzin, L. J.; Hoggard, A.; Shuang, B.; D. S. Indrasekara, A. S.; Chen, S.; Wang, L. Y.; Derry, P. J.; Liopo, A.; et al. Adsorption and Unfolding of a Single Protein Triggers Nanoparticle Aggregation. *ACS Nano* **2016**, *10*, 2103–2112.
- (29) Perham, M.; Halas, N. J.; Neumann, O.; Barhoumi, A.; Wittung-Stafshede, P.; Yuwono, V. M.; Zhang, D.; Wang, H.; Hartgerink, J. D. Gold Nanoparticles Can Induce the Formation of Protein-Based Aggregates at Physiological PH. *Nano Lett.* **2009**, *9*, 666–671.
- (30) Neupane, S.; Pan, Y.; Takalkar, S.; Bentz, K.; Farmakes, J.; Xu, Y.; Chen, B.; Liu, G.; Qian, S. Y.; Yang, Z. Probing the Aggregation Mechanism of Gold Nanoparticles Triggered by a Globular Protein. *J. Phys. Chem. C* **2017**, *121*, 1377–1386.
- (31) Shang, L.; Wang, Y.; Jiang, J.; Dong, S. PH-Dependent Protein Conformational Changes in Albumin:Gold Nanoparticle Bioconjugates: A Spectroscopic Study. *Langmuir* **2007**, *23*, 2714–2721.
- (32) Maity, M.; Das, S.; Maiti, N. C. Stability and Binding Interaction of Bilirubin on a Gold Nano-Surface: Steady State Fluorescence and FT-IR Investigation. *Phys. Chem. Chem. Phys.* **2014**, *16*, 20013–20022.
- (33) Vasquez, E. S.; Cunningham, J. L.; McMahan, J. B.; Simpson, C. L.; Walters, K. B. Fetuin-A Adsorption and Stabilization of Calcium Carbonate Nanoparticles in a Simulated Body Fluid. *J. Mater. Chem. B* **2015**, *3*, 6411–6419.
- (34) Surewicz, W. K.; Mantsch, H. H.; Chapman, D. Determination of Protein Secondary Structure by Fourier Transform Infrared Spectroscopy: A Critical Assessment. *Biochemistry* **1993**, *32*, 389–394.
- (35) Krimm, S. Vibrational Analysis of Conformation in Peptides, Polypeptides, and Proteins. *Biopolymers* **1983**, *22*, 217–225.
- (36) Lin, S. S.; Chen, I. C.; Yang, J.; Hsueh, T. J.; Hsu, C. L.; Lee, H. E.; Shieh, T. Y. A Study on One-Step Immobilization of Horse Immunoglobulin with Vertically Grown ZnO Nanorods Substrates. *J. Electrochem. Soc.* **2011**, *158*, K107–K111.

- (37) Kaur, K.; Forrest, J. A. Influence of Particle Size on the Binding Activity of Proteins Adsorbed onto Gold Nanoparticles. *Langmuir* **2012**, *28*, 2736–2744.
- (38) Chiu, N. F.; Huang, T. Y. Sensitivity and Kinetic Analysis of Graphene Oxide-Based Surface Plasmon Resonance Biosensors. *Sens. Actuators, B* **2014**, *197*, 35–42.
- (39) Aly, M. A.; Domig, K. J.; Kneifel, W.; Reimhult, E. Immunogold Nanoparticles for Rapid Plasmonic Detection of *C. Sakazakii*. *Sensors* **2018**, *18*, No. 2028.
- (40) Dong, A.; Huang, P.; Caughey, W. S. Protein Secondary Structures in Water from Second-Derivative Amide I Infrared Spectra. *Biochemistry* **1990**, *29*, 3303–3308.
- (41) Buijs, J.; Norde, W.; Lichtenbelt, J. W. T. Changes in the Secondary Structure of Adsorbed IgG and F(Ab')<sub>2</sub> Studied by FTIR Spectroscopy. *Langmuir* **1996**, *12*, 1605–1613.
- (42) Walter, D. Primary Particles–Agglomerates–Aggregates. Commission for the Investigation of Health Hazards of Chemical Compounds in the Work Area. *Nanomaterials* **2013**, *9*, 9–24.
- (43) Haller, E.; Lindner, W.; Lämmerhofer, M. Gold Nanoparticle-Antibody Conjugates for Specific Extraction and Subsequent Analysis by Liquid Chromatography-Tandem Mass Spectrometry of Malondialdehyde-Modified Low Density Lipoprotein as Biomarker for Cardiovascular Risk. *Anal. Chim. Acta* **2015**, *857*, 53–63.
- (44) Pandey, S. K.; Suri, C. R.; Chaudhry, M.; Tiwari, R. P.; Rishi, P. A Gold Nanoparticles Based Immuno-Bioprobe for Detection of Vi Capsular Polysaccharide of *Salmonella Enterica* Serovar Typhi. *Mol. Biosyst.* **2012**, *8*, 1853–1860.
- (45) Liao, J.; Zhang, Y.; Yu, W.; Xu, L.; Ge, C.; Liu, J.; Gu, N. Linear Aggregation of Gold Nanoparticles in Ethanol. *Colloids Surf., A* **2003**, *223*, 177–183.
- (46) James, A. E.; Driskell, J. D. Monitoring Gold Nanoparticle Conjugation and Analysis of Biomolecular Binding with Nanoparticle Tracking Analysis (NTA) and Dynamic Light Scattering (DLS). *Analyst* **2013**, *138*, 1212–1218.
- (47) Yüce, M.; Kurt, H. How to Make Nanobiosensors: Surface Modification and Characterisation of Nanomaterials for Biosensing Applications. *RSC Adv.* **2017**, *7*, 49386–49403.
- (48) Jans, H.; Austin, L.; Jans, H.; Liu, X.; Austin, L.; Maes, G.; Huo, Q. Dynamic Light Scattering as a Powerful Tool for Gold Nanoparticle Bioconjugation and Biomolecular Binding Studies. *Anal. Chem.* **2009**, *81*, 9425–9432.
- (49) Welch, N. G.; Scoble, J. A.; Muir, B. W.; Pigram, P. J. Orientation and Characterization of Immobilized Antibodies for Improved Immunoassays (Review). *Biointerphases* **2017**, *12*, No. 02D301.
- (50) Wang, A.; Perera, Y. R.; Davidson, M. B.; Fitzkee, N. C. Electrostatic Interactions and Protein Competition Reveal a Dynamic Surface in Gold Nanoparticle-Protein Adsorption. *J. Phys. Chem. C* **2016**, *120*, 24231–24239.
- (51) Khashayar, P.; Amoabediny, G.; Larijani, B.; Hosseini, M.; Vanfleteren, J. Fabrication and Verification of Conjugated AuNP-Antibody Nanoprobe for Sensitivity Improvement in Electrochemical Biosensors. *Sci. Rep.* **2017**, *7*, No. 16070.
- (52) Brewer, S. H.; Glomm, W. R.; Johnson, M. C.; Knag, M. K.; Franzen, S. Probing BSA Binding to Citrate-Coated Gold Nanoparticles and Surfaces. *Langmuir* **2005**, *62*, 9303–9307.
- (53) Bharti, B.; Meissner, J.; Findenegg, G. H. Aggregation of Silica Nanoparticles Directed by Adsorption of Lysozyme. *Langmuir* **2011**, *27*, 9823–9833.
- (54) Anderson, D. E.; Becktel, W. J.; Dahlquist, F. W. PH-Induced Denaturation of Proteins: A Single Salt Bridge Contributes 3-5 Kcal/Mol to the Free Energy of Folding of T4 Lysozyme. *Biochemistry* **1990**, *29*, 2403–2408.
- (55) Kong, J.; Yu, S. Fourier Transform Infrared Spectroscopic Analysis of Protein Secondary Structures. *Acta Biochim. Biophys. Sin.* **2007**, *39*, 549–559.
- (56) Huy, T. Q.; Hanh, N. T. H.; Van Chung, P.; Anh, D. D.; Nga, P. T.; Tuan, M. A. Characterization of Immobilization Methods of Antiviral Antibodies in Serum for Electrochemical Biosensors. *Appl. Surf. Sci.* **2011**, *257*, 7090–7095.
- (57) Barth, A. Infrared Spectroscopy of Proteins. *Biochim. Biophys. Acta, Bioenerg.* **2007**, *1767*, 1073–1101.
- (58) Huy, T. Q.; Hanh, N. T. H.; Thuy, N. T.; Van Chung, P.; Nga, P. T.; Tuan, M. A. A Novel Biosensor Based on Serum Antibody Immobilization for Rapid Detection of Viral Antigens. *Talanta* **2011**, *86*, 271–277.
- (59) Thomas, D. B.; McGoverin, C. M.; McGraw, K. J.; James, H. F.; Madden, O. Vibrational Spectroscopic Analyses of Unique Yellow Feather Pigments (Spheniscins) in Penguins. *J. R. Soc. Interface* **2013**, *10*, 1–9.
- (60) Marsich, L.; Bonifacio, A.; Mandal, S.; Krol, S.; Beleites, C.; Sergio, V. Poly-L-Lysine-Coated Silver Nanoparticles as Positively Charged Substrates for Surface-Enhanced Raman Scattering. *Langmuir* **2012**, *28*, 13166–13171.
- (61) Geddes, N. J.; Paschinger, E. M.; Furlong, D. N.; Caruso, F.; Hoffmann, C. L.; Rabolt, J. F. Surface Chemical Activation of Quartz Crystal Microbalance Gold Electrodes-Analysis by Frequency Changes, Contact Angle Measurements and Grazing Angle FTIR. *Thin Solid Films* **1995**, *260*, 192–199.
- (62) Surewicz, W. K.; Mantsch, H. H. New insight into protein secondary structure from resolution-enhanced infrared spectra. *Biochim. Biophys. Acta, Protein Struct. Mol. Enzymol.* **1988**, *952*, 115–130.
- (63) Goormaghtigh, E.; Ruyschaert, J. M.; Raussens, V. Evaluation of the Information Content in Infrared Spectra for Protein Secondary Structure Determination. *Biophys. J.* **2006**, *90*, 2946–2957.
- (64) Giacomelli, C. E.; Bremer, M. G. E. G.; Norde, W. ATR-FTIR Study of IgG Adsorbed on Different Silica Surfaces. *J. Colloid Interface Sci.* **1999**, *220*, 13–23.
- (65) Prestrelski, S. J.; Tedeschi, N.; Arakawa, T.; Carpenter, J. F. Dehydration-Induced Conformational Transitions in Proteins and Their Inhibition by Stabilizers. *Biophys. J.* **1993**, *65*, 661–671.
- (66) Xu, Y.; Sherwood, J.; Qin, Y.; Crowley, D.; Bonizzoni, M.; Bao, Y. The Role of Protein Characteristics in the Formation and Fluorescence of Au Nanoclusters. *Nanoscale* **2014**, *6*, 1515–1524.
- (67) Reiter, G.; Hassler, N.; Weber, V.; Falkenhagen, D.; Fringeli, U. P. In Situ FTIR ATR Spectroscopic Study of the Interaction of Immobilized Human Tumor Necrosis Factor- $\alpha$  with a Monoclonal Antibody in Aqueous Environment. *Biochim. Biophys. Acta, Proteins Proteomics* **2004**, *1699*, 253–261.
- (68) Tang, J.; Luan, F.; Chen, X. Binding Analysis of Glycyrrhetic Acid to Human Serum Albumin: Fluorescence Spectroscopy, FTIR, and Molecular Modeling. *Bioorg. Med. Chem.* **2006**, *14*, 3210–3217.
- (69) Shipway, A. N.; Lahav, M.; Gabai, R.; Willner, I. Investigations into the Electrostatically Induced Aggregation of Au Nanoparticles. *Langmuir* **2000**, *16*, 8789–8795.
- (70) Ji, Z.; Suarez, E.; Wang, X.; Meng, H.; Tian, X.; Saji, G.; Jin, X.; Zhang, H.; Hoek, E. M. V.; Godwin, H.; et al. Dispersion and Stability Optimization of TiO<sub>2</sub> Nanoparticles in Cell Culture Media. *Environ. Sci. Technol.* **2014**, *44*, 7309–7314.
- (71) De Temmerman, P. J.; Van Doren, E.; Verleysen, E.; Van der Stede, Y.; Francisco, M. A. D.; Mast, J. Quantitative Characterization of Agglomerates and Aggregates of Pyrogenic and Precipitated Amorphous Silica Nanomaterials by Transmission Electron Microscopy. *J. Nanobiotechnol.* **2012**, *10*, 1–11.
- (72) Schiffer, H. A.; Lee, G. Single-Droplet Evaporation Kinetics and Particle Formation in an Acoustic Levitator. Part 2: Drying Kinetics and Particle Formation from Microdroplets of Aqueous Mannitol, Trehalose, or Catalase. *J. Pharm. Sci.* **2007**, *96*, 2284–2295.
- (73) He, Y.; Xu, J.; Pan, X. A statistical approach to the prediction of pKa values in proteins. *Proteins* **2007**, *45*, 75–82.
- (74) Domingos, R. F.; Wilkinson, K. J.; Baalousha, M. A.; Ju-Nam, Y.; Lead, J. R.; Reid, M. M.; Tufenkji, N.; Leppard, G. G. Characterizing Manufactured Nanoparticles in the Environment: Multimethod Determination of Particle Sizes. *Environ. Sci. Technol.* **2009**, *43*, 7277–7284.